Journal of
Synchrotron Radiation
ISSN 0909-0495

Received 25 August 2006
Accepted 12 December 2006

Chemically selective soft X-ray patterning of polymers

Jian Wang,[a] Harald D. H. Stöver,[a] Adam P. Hitchcock[a]* and Tolek Tyliszczak[b]

[a]Department of Chemistry and Brockhouse Institute for Materials Research, McMaster University, Hamilton, ON, Canada L8S 4M1, and [b]Advanced Light Source, Lawrence Berkeley National Laboratory, Berkeley, CA 94720, USA. E-mail: aph@mcmaster.ca

The chemically selective modification of polymer mixtures by monochromated soft X-rays has been explored using the high-brightness fine-focused 50 nm beam of a scanning transmission X-ray microscope. Four different polymer systems were examined: a polymethylmethacrylate (PMMA) polyacrylonitrile (PAN) bilayer film; a PMMA-*blend*-PAN microphase-separated film; a poly(MMA-*co*-AN) copolymer film; and a poly(ethyl cyanoacrylate) homopolymer film. A high level of chemically selective modification was achieved for the PMMA/PAN bilayer; in particular, irradiation at 288.45 eV selectively removed the carbonyl group from PMMA while irradiation at 286.80 eV selectively reduced the nitrile group of PAN, even when these irradiations were carried out at the same (x,y) position of the sample. In the last two homogenous polymer systems, similar amounts of damage to the nitrile and carbonyl groups occurred during irradiation at either 286.80 or 288.45 eV. This is attributed to damage transfer between the C≡N and C═O groups mediated by primary electrons, secondary electrons or radical/ionic processes, aided by their close spatial proximity. Although the overall thickness of the bilayer sample at 70 nm is smaller than the lateral line spreading of 100 nm, the interface between the layers appears to effectively block the transport of energy, and hence damage, between the two layers. The origins of the line spreading in homogeneous phases and possible origins of the damage blocking effect of the interface are discussed. To demonstrate chemically selective patterning, high-resolution multi-wavelength patterns were created in the PMMA/PAN bilayer system.

Keywords: soft X-ray; lithography; chemically selective; radiation damage; C 1*s* NEXAFS; PMMA; PAN; PECA.

1. Introduction

Current sub-micrometer and nanolithography techniques, such as X-ray or extreme ultraviolet projection lithography (Cerrina, 2000; Stulen & Sweeney, 1999), electron or ion beam lithography (Tseng *et al.*, 2003; Melngailis *et al.*, 1998), nanoimprint lithography (Guo, 2004) and scanning probe microscope-based lithography (Tseng *et al.*, 2005), do not explicitly use chemically selective interactions with multiple resist materials during pattern writing. Patterning processes can be classified into two categories: negative photoresists, which involve cross-linking, and positive photoresists, which involve main-chain scission and mass loss. All of these phenomena are a direct consequence of radiation damage to the polymers, the details of which depend on the kind of radiation used in the pattern-forming step of the lithography. However, in all methods developed to date the radiation damage is non-specific with respect to the chemical nature of the resist materials, and thus the patterning process is not chemically specific. Here we introduce a novel method that has the potential to add chemical selectivity to lithography, specifically the use of chemically selective X-ray absorption coupled with a specific substrate structure to confine the pattern (radiation damage) to specific chemical species. Many conventional resist polymers contain functional groups that have very strong resonant absorption at specific X-ray energies in the soft X-ray region (100–1000 eV). These may thus serve as a basis for chemically selective lithography, if appropriate multi-component substrate fabrication and exposure techniques can be developed. The nano-patterning technique demonstrated in this work may have potential applications in the manufacture of custom electronic circuits, micro-reactors and other types of nanofabrication.

Rates and mechanisms of radiation damage are important in many areas of science and technology and have been studied extensively (Weik *et al.*, 2000; Cherezov *et al.*, 2002; Sanche, 2002; Pease, 2003; Osetsky & Bacon, 2003; Trachenko, 2004; Sagstuen *et al.*, 2004; Cadet *et al.*, 2005; Joers *et al.*, 2006).

There are many aspects to radiation damage, such as the electronic and structural changes associated with the primary energy deposition; subsequent secondary processes associated with free electrons, inelastically scattered electrons, and radical or ionic fragments; transport processes of the products of the primary and secondary events; and ultimately thermal or chemical reactions such as oxidation and depolymerization. The aspect of radiation damage that is critical in any situation depends on the reason for carrying out a potentially damaging radiation exposure, and the sensitivity of subsequent measurements to the consequences of the damage. A hierarchy of effects ordered by increasing dose might be: biological viability, long-range structural change, short-range chemical change, mass loss. The focus of this work is chemical change since this is the basis for chemically selective lithography.

Radiation damage is a common and critical phenomenon in high-spatial-resolution X-ray microscopy (Rightor *et al.*, 1997; Zhang *et al.*, 1995; Beetz & Jacobsen, 2003; Coffey *et al.*, 2002). As soft X-ray microscopy techniques such as scanning transmission X-ray microscopy (STXM) (Ade, 1998; Ade & Urquhart, 2002) and X-ray photoelectron emission microscopy (X-PEEM) (Bauer, 2001) are applied increasingly frequently to radiation-sensitive polymer and biological samples (Koprinarov *et al.*, 2001; Hitchcock *et al.*, 2002; Morin *et al.*, 2004), it is important to understand both the nature and the rate of radiation damage by soft X-rays in order to achieve chemically meaningful microanalysis. Optimal strategies for acquisition of detailed spectroscopy, quantitative determination of radiation damage kinetics, and a better understanding of damage mechanisms by soft X-rays are not only significant for soft X-ray spectromicroscopy analysis, but are also the foundations for the development of chemically selective patterning or lithography. Jacobsen and co-workers have made several quantitative studies of radiation damage in the Stony Brook STXM at NSLS, including quantitative studies of the damage rate for polymethylmethacrylate (PMMA) at room and liquid-nitrogen temperatures and at both the C 1*s* and O 1*s* edges (Zhang *et al.*, 1995; Beetz & Jacobsen, 2003). Coffey *et al.* (2002) also used C 1*s* near-edge X-ray absorption spectroscopy (NEXAFS) recorded in STXM to study radiation chemistry of a series of common polymers that contain the carbonyl functional group. They all used a first-order kinetics model to characterize radiation damage in terms of a critical radiation dose parameter, which is the dose required to attenuate the intensity of a specific spectroscopic feature to (1/e) or 37% of its initial value.

Here we present the results of a study aimed at optimizing the sample composition, structure and procedures for chemically selective patterning of polymers by monochromatic soft X-rays. The desired polymer materials should have strong, sharp, distinct characteristic absorption peaks such as $1s \rightarrow \pi^*$ transitions, which are shifted by at least 1 eV with respect to each other. There should also be a suitable damage rate in terms of a relatively low critical dose and a high molecular weight (>100 kDa) for better film-forming capability. Both the irradiation and the subsequent chemical analysis are performed using a ~50 nm focused beam in an interferometrically controlled scanning transmission X-ray microscope (Kilcoyne *et al.*, 2003). In this study, two polymer species, PMMA and polyacrylonitrile (PAN), were first independently measured with monochromated soft X-rays to acquire NEXAFS spectra and radiation damage information. The absorption spectra are characterized by a strong C $1s \rightarrow \pi^*_{C=O}$ absorption peak at 288.4 eV for PMMA and a strong C $1s \rightarrow \pi^*_{C\equiv N}$ absorption peak at 286.8 eV for PAN. Subsequently, chemically selective X-ray patterning was explored by using specific X-ray photon energies and radiation doses to confine the radiation damage at 288.4 eV to the C=O groups of PMMA and that at 286.8 eV to the C≡N groups of PAN. Four different mixed polymer film systems were then evaluated, with different spatial scales separating the carbonyl and nitrile groups: a PMMA-*on*-PAN bilayer film, a PMMA-*blend*-PAN microphase-separated film, a poly(MMA-*co*-AN) copolymer film and a poly(ethyl cyanoacrylate) (PECA) homopolymer film. The chemical structures of PMMA, PAN and PECA are illustrated in the scheme below. Energy-specific damage of C=O in PMMA at 288.4 eV and C≡N in PAN at 286.8 eV at the same (x,y) position of the sample was achieved only for the PMMA/PAN bilayer. The reasons for the failure in the other three cases, and the success in the bilayer are discussed. To demonstrate chemically selective patterning, several chemically selective patterns were created in the PMMA/PAN bilayer system.

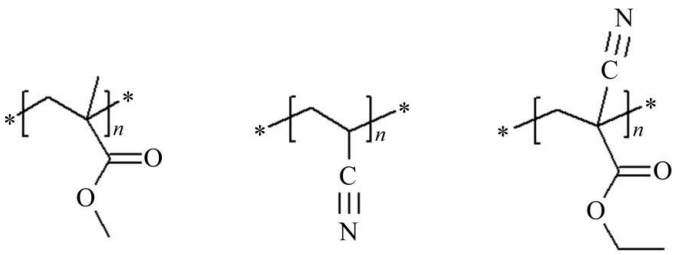

This paper is organized as follows. After describing experimental methods, the NEXAFS spectra for pure PMMA, pure PAN and four polymer film systems are presented. Then the chemical selectivity in radiation damage of the four different polymer film systems is presented. This is followed by demonstrations of chemically selective patterning in the PMMA/PAN bilayer system and a discussion of the physicochemical basis for the observations.

2. Experimental

2.1. Sample preparation

PMMA (M_w = 312 K, polydispersity index PDI = M_w/M_n = 1.01) was obtained from Polymer Source Inc. and PAN (M_w = 150 K) was obtained from Aldrich. Both were used without further purification. Free-standing films of the single polymers were made according to the following procedure. A 1 wt.% toluene solution of PMMA was prepared using anhydrous

toluene (Aldrich, 99.8%). Then a 50 µl drop was spun-cast (3000 r.p.m., 30 s) onto a freshly peeled mica surface of 2.5 cm × 2.5 cm. The film was dried in ambient atmosphere for 5 min and cut into 3 mm × 3 mm pieces on the mica surface, and then floated onto milli-Q water. A piece of the polymer was then transferred from the water surface to a degreased hexacomb grid, then was dried again in ambient atmosphere before being used for STXM measurements. For the single or multilayer films involving PAN, the solvent was dimethyl formamide (DMF) and the spun-cast PAN on mica was dried under vacuum at 343 K for 0.5 h to remove all of the DMF. The single-layer film thickness was 30–40 nm according to STXM measurements under the above conditions. Free-standing bilayer films of PMMA (upper) and PAN (lower) were fabricated by spin-coating PMMA from toluene onto a dried PAN film prepared as described above. Reversing the spin-coating sequence of the two polymers produced a microphase-separated film, PMMA-*blend*-PAN, owing to re-dissolution of the first-cast PMMA layer in the DMF solvent.

Poly(MMA-*co*-AN) was synthesized by free-radical co-polymerization (Ekpenyong & Okonkwo, 1983). Ethyl cyano-acrylate was obtained commercially (Instant Krazy Glue, Elmer's Products Inc. and Toagosei Co. Ltd) and polymerized on a glass slide by exposure to air to form PECA. A few milligrams of each sample were dissolved in toluene, then a 50 µl drop was placed on a Si_3N_4 window [750 µm × 750 µm window back-etched into a 7.5 mm × 7.5 mm × 200 µm silicon wafer chip coated with 75 nm of Si_3N_4 (Silson Ltd)]. When the solvent evaporated, polymer particles and film pieces were deposited on the Si_3N_4 surface. Thin uniform-thickness regions sufficiently large (1–2 µm) for the semi-quantitative radiation damage studies were found on these highly heterogeneous samples. A PECA film, uniform over a 10 µm × 10 µm area, was prepared by ultramicrotoming a solid block to form 60 nm-thick uniform films.

2.2. STXM

Experiments were performed using STXM at beamline 5.3.2 at the Advanced Light Source (Kilcoyne *et al.*, 2003; Warwick *et al.*, 2002). STXM uses a Fresnel zone plate to focus X-rays to a ∼50 nm point probe. The sample is raster scanned through the focused X-ray spot with synchronized detection of transmitted X-rays to measure the energy-dependent absorption by a volume pixel of material. The contrast in STXM images depends strongly on the nature of the chemical constituents and the X-ray energy; the dominant image-contrast mechanism is the variation of the inner-shell excitation or NEXAFS spectra of the constituents, although density and thickness distributions are also important. Radiation damage of the PMMA and PAN polymer samples was clearly observed when the accumulated exposure of the beam on a given spot of the sample (either in a single dwell or multiple shorter exposures) was larger than ∼100 ms with typical photon fluxes of 2–3 MHz in the focused spot. The dispersive entrance slit and both the dispersive and non-dispersive exit slits of the monochromator were adjusted to control the photon flux and dose rate on the sample. In STXM532 the entrance and dispersive exit slit control the energy resolution, while the combination of the two exit slits controls the spatial resolution. Since we form patterns using X-ray energies corresponding to strong relatively narrow absorption lines of the components, there is potentially some interplay between the energy resolution and the quantitative rates of pattern formation. However, in this case the energy resolution under even the least monochromated conditions (∼0.4 eV) is smaller than the resonance width (0.8–1.2 eV). Similarly, as discussed in detail later, the spatial resolution of our patterns (150–200 nm) is much worse than the spatial resolution of the microscope [40 nm with standard slits settings (60/30/30 µm) and 60 nm with the enlarged slits used for pattern writing (80/40/40) (Kilcoyne *et al.*, 2003)]. The line broadening is controlled by factors other than the exit slit settings. The damaged region was analyzed by imaging it at the photon energy giving the best contrast of the damaged material relative to the undamaged material, which was at the strong C 1*s* → π* transitions (286.8 eV for PAN and 288.4 eV for PMMA). The NEXAFS spectra of the damaged and undamaged regions were acquired using an image sequence [stack (Jacobsen *et al.*, 2000)] with much lower photon flux. Reference spectra on absolute linear absorbance scales [*i.e.* optical density (OD) per nm thickness sample] were derived by scaling the spectra of the undamaged material to the X-ray absorption response in the regions of 275–282 eV and 320–350 eV, to match that of the linear X-ray absorption for the elemental composition of the sample derived from literature absorption coefficients (Henke *et al.*, 1993).

For STXM quantitative microanalysis, the Beer–Lambert law is obeyed, so the OD of a sample at any photon energy can be expressed as

$$\mathrm{OD} = -\ln(I/I_0) = \mu\rho l, \quad (1)$$

where I and I_0 are the transmitted and incident X-ray photon flux, respectively, μ is the energy-dependent mass absorption coefficient, ρ is the polymer density, and l is the sample thickness. For radiation damage evaluation, the approach is to find the relationship between the damage in terms of OD change and the absorbed radiation dose a [in units of grays (Gy), where 1 Gy = 1 J kg^{-1}]. The dose (a) was obtained from

$$a = FEt/m = (I_0 - I)Et/m = I_0[1 - \exp(-\mathrm{OD})]Et/m, \quad (2)$$

where F is the absorbed flux (absorbed photons per second) of a specific volume pixel (voxel), which is derived from the incident flux (I_0) and the OD at the exposure photon energy using equation (1), E is the photon energy, t is the exposure time and m is the mass of the voxel. The incident flux is measured in the absence of the sample and is corrected for the measured detector efficiency [30 ± 10% in the C 1*s* region (Kilcoyne *et al.*, 2003)]. A N_2 gas filter was used to ensure that the incident photon beam contained negligible higher-order components. This can be quite important in quantitative dose-damage studies for polymers containing N or O since the second-order photons impart a larger amount of energy per

absorbed photon and since there is a significant absorbance at the second-order energy.

In order to determine the critical dose for damage of a specific material from the measured damage-exposure data, the damage *versus* dose data were fit to postulated rate laws, such as a first-order kinetic process (Zhang *et al.*, 1995; Beetz & Jacobsen, 2003; Coffey *et al.*, 2002) which appears to be suitable in these cases where mass loss is relatively small and the damage is mainly chemical change,

$$D = D_\infty + A\exp(-a/a_c), \tag{3}$$

where D is a relative measure of damage (*e.g.* the OD change at a damage sensitive energy), D_∞ is the absorbance that remains after the damage process saturates, A is a constant, a is the dose, and a_c is the first-order constant or the critical dose, which is the dose that attenuates a specific spectroscopic feature to 37% of its initial value. The detailed quantitative dose-damage evaluation for PMMA and other materials has been presented elsewhere (Wang *et al.*, 2007). Here we focus on radiation damage selectivity for different two-component polymer samples, and how to achieve chemically selective patterning.

The chemically selective patterning experiments were performed using a pattern generation program, incorporated into *STXM_control*, the microscope control and data-acquisition software. In this mode the sample is positioned with ~10 nm precision under laser interferometer control, to predefined (x,y) locations and then a fast-acting (~300 µs) in-vacuum piezo shutter is opened for a precise predefined position-dependent time interval to expose the sample to the flux of monochromated X-rays. With the slits typically used for pattern generation (80/40/40 µm), the energy resolution is ~400 meV and the spatial resolution is ~60 nm (Kilcoyne *et al.*, 2003). Input files for pattern generation consist of lists of (x,y,t,E) values for each pixel which are generated using routines in *aXis2000* (http://unicorn.mcmaster.ca/aXis2000.html). For multi-color patterns (exposures at multiple photon energies), color images are color separated and the individual components are used to generate pattern files for each color.

3. Results

3.1. Radiation damage for PMMA and PAN

The C 1*s* NEXAFS spectra for undamaged and heavily radiation damaged PMMA and PAN are presented in Fig. 1. For undamaged PMMA, the spectrum is characterized by the sharp strong C 1*s* $\rightarrow \pi^*_{C=O}$ transition at 288.45 eV; there are additional features at 292, 296 and 302 eV, arising from various C 1*s* $\rightarrow \sigma^*$ transitions, with that at 302 eV corresponding to C 1*s* $\rightarrow \sigma^*_{C=O}$ excitations. For heavily damaged PMMA, the 288.45 eV and 302 eV features disappear, and a new feature appears at 285 eV. (Note, for simplicity, when referring to the damage energy of PMMA we state 288.4 eV in the following, but this should be understood to be the $\pi^*_{C=O}$ peak maximum of 288.45 eV.) The 288.4 eV and 302 eV features disappear since the carbonyl and associated ester oxygen are removed by decarboxylation (ejection of CO_2). The 285 eV signal, which is associated with C 1*s* $\rightarrow \pi^*_{C=C}$ transitions, arises from C=C bonds formed in damaged parts of the polymer backbone. There is also considerable mass loss as indicated by the ~30% reduction of the C 1*s* continuum intensity. The significantly reduced absorption at energies below 284 eV in the damaged sample is consistent with a large loss of oxygen since the pre-C1*s* absorption is stronger for higher-Z elements.

The major spectral feature in the spectrum of undamaged PAN is the strong C 1*s* $\rightarrow \pi^*_{C\equiv N}$ absorption peak at 286.80 eV. This signal decreases as PAN is radiation damaged, in part owing to loss of CN (although there is much less mass loss in PAN than in PMMA) and in part owing to transformation of the C≡N triple bond to a C=N double bond or C—N single bond. Note that the associated $\sigma^*_{C\equiv N}$ transition at 306 eV is lost and there is the appearance of a broad peak at 301 eV which is likely associated with C 1*s* $\rightarrow \sigma^*_{C=N}$ transitions in the transformed material. With damage to PAN there is growth of a new feature at 285 eV, which is also associated with unsaturation in the polymer backbone, as in damaged PMMA. The intensity decrease in the continuum, *i.e.* the spectroscopic region above the inner-shell ionization potential, usually reflects mass loss upon radiation damage (Coffey *et al.*, 2002). Fig. 1 shows that PMMA undergoes apparent mass loss for completely radiation damaged as the continuum regime intensity decreases. For PAN the situation is different; there is

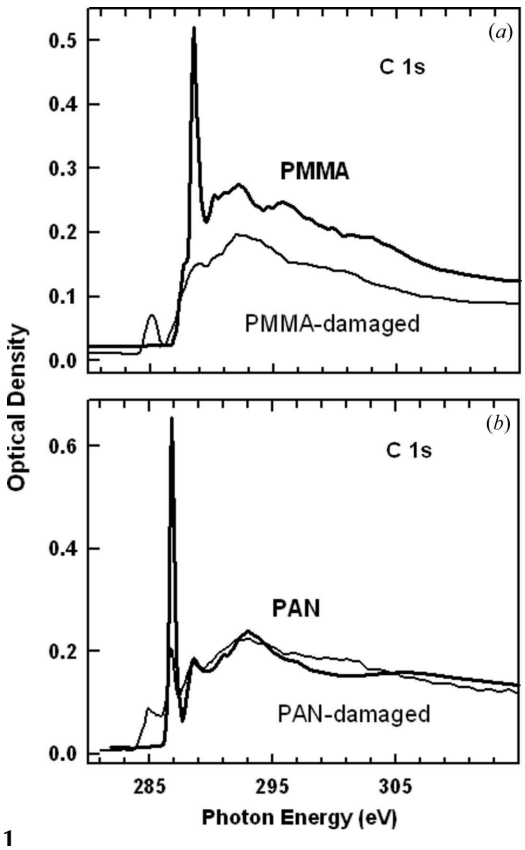

Figure 1
C 1*s* near-edge X-ray absorption fine structure (NEXAFS) spectra of undamaged and damaged PMMA (*a*) and PAN (*b*).

relatively little change in the C 1*s* continuum in the dose regime examined. This suggests that PAN does not suffer much mass loss during radiation damage.

Under similar irradiation conditions (incident photon flux, dose rate and comparable sample thickness *etc.*) the critical dose in terms of the change of the PMMA $\pi^*_{C=O}$ feature (destruction and loss of C═O groups) was determined to be $(\sim 60 \pm 8) \times 10^6$ Gy, while that of PAN associated with the change of the PAN $\pi^*_{C\equiv N}$ feature (destruction and loss of C≡N groups) was $(150 \pm 20) \times 10^6$ Gy. The critical dose of PMMA we have determined is comparable with the literature values (Zhang *et al.*, 1995; Coffey *et al.*, 2002), so the relative rate and sensitivity of the radiation damage for PMMA *versus* PAN are reliably estimated by these critical doses. The critical dose ratio was the factor used to determine the optimum exposure protocol for chemically selective damage or patterning of the samples containing the two functional groups. Detailed quantitative evaluation of the critical dose, comparison with literature values, and a discussion of the radiation chemistry of PMMA has been presented elsewhere (Wang *et al.*, 2007).

3.2. Chemically selective radiation damage

Given the large X-ray absorption coefficients of PAN and PMMA at their respective π^* resonance energies, one might naively expect that it would be possible to confine the damage to one or the other species by using monochromatic X-rays of corresponding energies. However, it is not only the initial deposition of energy that is important, but also the cascade of secondary processes (Cazaux, 1997). In fact, as shown below, it is a real challenge to retain the selectivity of the initial energy deposition process, and thereby achieve chemically selective X-ray radiation damage. We have explored this issue by examining four different polymer film systems which have different spatial scales separating carbonyl and nitrile groups: a PMMA-*on*-PAN bilayer film, a PMMA-*blend*-PAN micro-phase-separated film, a poly(MMA-*co*-AN) copolymer film and a PECA homopolymer film. Fig. 2 shows the C 1*s* NEXAFS spectra of three of these samples. The spectrum of the PMMA-*blend*-PAN sample is not included in Fig. 2 since that sample phase separated and thus contains distinct domains of essentially pure PMMA and PAN, which have C 1*s* spectra as given in Fig. 1. The PMMA/PAN bilayer film has the same π^* peak positions as single-layer PMMA (288.45 eV) and PAN (286.80 eV), but the ratio of the intensity of the $\pi^*_{C=O}$ to the $\pi^*_{C\equiv N}$ peak is higher, since the PMMA layer is thicker than the PAN layer. The π^* peak positions of poly(MMA-*co*-AN) are also the same as pure PMMA and pure PAN. Although this statistical copolymer may be nm-scale heterogeneous, at the scale of the STXM spatial resolution (50 nm) it is effectively homogeneous. The energies of the π^* peaks in the PECA sample are slightly different from those in PMMA and PAN. In particular, the C 1*s* $\rightarrow \pi^*_{C=O}$ feature (288.58 eV) is 0.13 (3) eV higher in energy than its counterpart in PMMA and the $\pi^*_{C\equiv N}$ feature (286.68 eV) is 0.12 (3) eV lower than its counterpart in PAN. These small but real chemical shifts are due to the electronic interaction between the carbonyl and nitrile groups since the two unsaturated functional groups are connected to the same carbon atom and thus their molecular orbitals interact (Stöhr, 1992).

The procedure initially used to explore chemically selective radiation damage consisted of writing lines at selected photon energies into a thin film of each system with the same slit settings and same dwell time per pixel. The four photon energies were 285.15 eV (neither species absorbs), 286.80 eV (only PAN absorbs), 288.45 eV (mainly PMMA absorbs, with a small PAN contribution) and 290.0 eV (both absorb) (note that the STXM532 energy scale is defined meaningfully to within 0.02 eV, and the PAN and PMMA peak energies are accurate to within 0.05 eV). Following this exposure sequence the region of the four lines was imaged at the same four photon energies to evaluate the radiation damage. Fig. 3 presents optical density images at the four photon energies, for the PMMA-*on*-PAN bilayer, the poly(MMA-*co*-AN) co-polymer film and the PECA homopolymer film. The dark lines in the images at 286.8, 288.4 and 290 eV correspond to a decrease of optical density as radiation damage occurs, while the bright lines in the 285.1 eV image indicate increased optical density, associated with formation of C═C bonds in the polymer backbone upon radiation damage. Energy-specific damage of C≡N in PAN and C═O in PMMA was clearly achieved for the PMMA/PAN bilayer for irradiation at the respective absorption peaks. In that case, in the image recorded at 286.8 eV the line drawn at 286.8 eV is very dark, corresponding to the exposure at that energy. However, there is very little damage (only a faint line) at the same location in

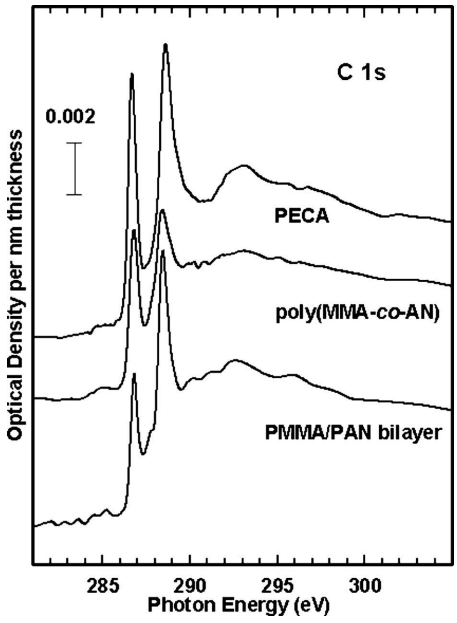

Figure 2
C 1*s* absolute linear absorption NEXAFS spectra (*i.e.* optical density per nm thickness sample) of PMMA-*on*-PAN bilayer, poly(MMA-*co*-AN) and PECA. These spectra were derived by scaling the originally recorded spectra to match that of the linear X-ray absorption for the elemental composition of the sample derived from literature absorption coefficients (Henke *et al.*, 1993).

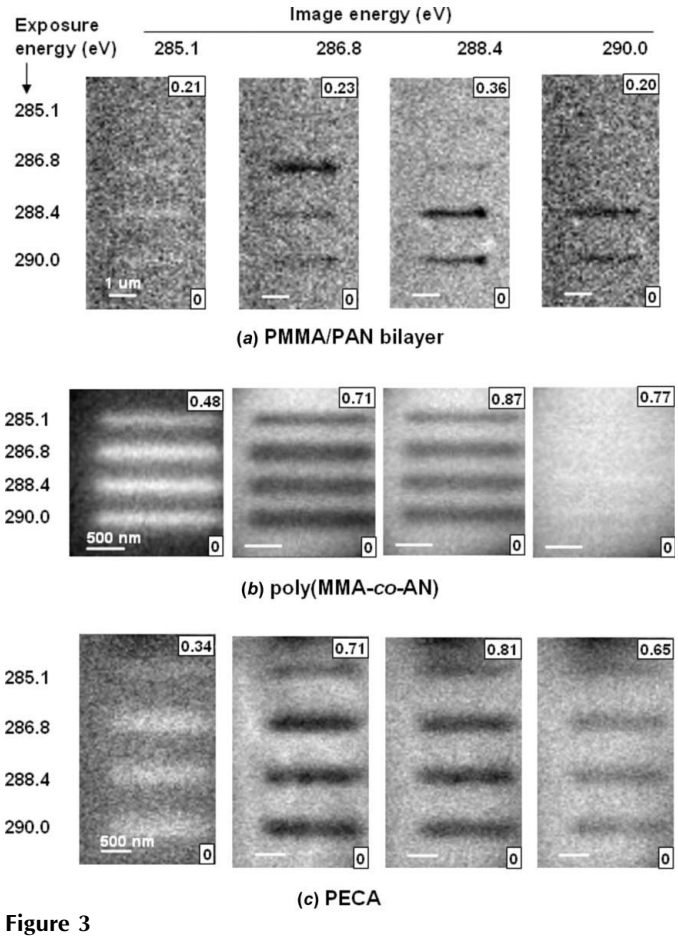

Figure 3
Optical density images of radiation damage of (*a*) PMMA/PAN bilayer, (*b*) poly(MMA-*co*-AN) and (*c*) PECA. These images are actually relative optical density images, which were converted from their transmission images by normalization to the maximum intensity of each individual transmission image. Four lines were exposed with the same slit settings, dwell time per pixel and pixel spacing, at four photon energies, respectively: 285.1 eV (neither species absorbs), 286.8 eV (only PAN absorbs), 288.4 eV (mainly PMMA absorbs, with a small PAN contribution) and 290.0 eV (both species absorb). The region of the sample exposed in this way was that imaged at the same four photon energies to evaluate the selectivity of radiation damage.

the image recorded at 288.4 eV. Similarly, in the image at 288.4 eV the line drawn at 288.4 eV is very dark corresponding to the exposure at that energy, while there is only a very faint damage line at the same location in the image at 286.8 eV. Thus we have demonstrated chemically selective damage for PAN and PMMA based on their differential absorption. Note that for this bilayer sample there is very little damage at the line exposed at 285.1 eV, while the line exposed at 290.0 eV results in damage that was imaged at both 286.8 and 288.4 eV indicating non-selective damage of the sample at 290 eV where both chemical species absorb relatively strongly. In the other two systems, similar amounts of damage to the nitrile and carbonyl groups occurred at 286.8 and 288.4 eV as indicated by the presence of two dark lines in each of the images at 286.8 and 288.4 eV. Exposure at 285.1 and 290.0 eV did not show any selective damage in these two samples. The failure to achieve chemically selective damage in the poly(MMA-*co*-AN) and PECA films is attributed to the close spatial proximity of the C≡N and C═O functional groups such that there is facile transfer of the initially absorbed energy between species *via* electrons and/or radicals and ions.

The range of damage spreading in PAN and PMMA was explored in the PMMA-*blend*-PAN microphase-separated film sample. Figs. 4(*a*) and 4(*b*) presents OD images at 286.8 and 288.4 eV for the same area of the sample. The contrast reversal indicates that, in this region of the sample, the continuous phase is PAN, while the isolated domains are PMMA. Note that other regions of the spun-cast film had the reverse phase segregation morphology, which was dictated by the local composition of the fluid as the DMF solvent evaporated. The full width at half-maximum (FWHM) of each line was derived by averaging orthogonal line profiles over a range of the line in each material. These FWHM values are then used as a measure of the range of damage migration under each condition in each material. The line width as a function of radiation dose for PMMA and PAN is plotted in Fig. 4(*c*). The width and thus the damage migration range increases in a non-linear fashion with increased radiation dose from ∼100 nm to ∼250 nm in PMMA and to a value above 300 nm in PAN. For the same dose the damage lines in PAN are noticeably wider than those of PMMA. The differences between line broadening in PAN and PMMA are more apparent when the line width is plotted as a function of ratio-to-critical dose (Fig. 4*d*) (the critical dose values used were 60×10^6 Gy for PMMA and 150×10^6 Gy for PAN). The increase in line width with increasing absorbed dose is roughly exponential, with an offset, suggesting that a pseudo-first-order kinetics model might be applicable. The offset value of 100–120 nm is rather larger than that expected from the spatial resolution of the STXM (50 nm). We interpret this in terms of a short-range low-dose damage process (perhaps the damage induced by photoelectron and high-energy secondary electrons) which occurs in addition to a slower longer-range damage spreading mechanism which may be radical/ion diffusion and depolymerization or some other effect (see §4). From Fig. 4(*c*) and especially Fig. 4(*d*), it would appear that the fit lines for the PAN and PMMA data are converging at the lowest dose to a value of ∼120 nm. This suggests the short-range damage mechanism might be relatively similar in the two materials but that the long-range damage transport mechanisms differ appreciably (or there may be a similar mechanism but with very different rates for the two materials).

3.3. Chemically selective patterning

The selectivity of damage to PAN and PMMA in the PMMA-*on*-PAN bilayer forms the basis for chemically selective soft X-ray patterning. The results described above were used to identify the X-ray photon energies and exposures that produce good contrast in each chemical component with least damage to the other component. Exposure can be controlled by adjusting either (or both) incident flux (by changing slits) or dwell time. The exposure times used were chosen such that the radiation dose for PAN (at 286.8 eV) was 2.5 times that for PMMA (at 288.4 eV) in order to use the same fraction of the

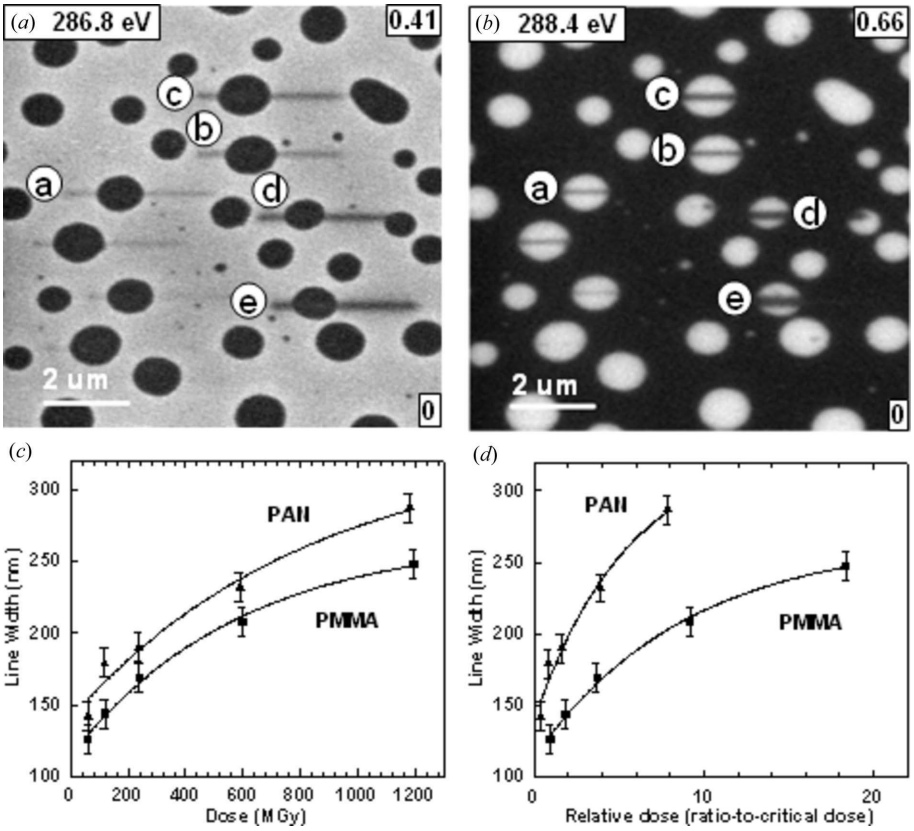

Figure 4
Evaluation of radical migration in a PMMA-*blend*-PAN microphase-separated film. (*a*) Optical density image at 286.8 eV (PAN is white). (*b*) Optical density image of the same region at 288.4 eV (PMMA is white). The lines labeled *a*, *b*, *c*, *d*, *e* were exposed to various doses at 320 eV prior to recording these images. (*c*) Plot of the average width of the damage lines in the PAN and PMMA material as a function of the dose. The data points are the measured line width (FWHM) at the indicated radiation doses for PMMA and PAN, respectively. The lines are fits of those data points to $w = w_o + a \exp(d/d_c)$. (*d*) Plot of the average width of the damage lines in the PAN and PMMA material as a function of ratio-to-critical dose (60×10^6 Gy for PMMA, 150×10^6 Gy for PAN).

critical dose of each species. Patterns at each energy were written by sequentially positioning the sample at the focused X-ray beam at a set of pre-defined points and exposing for a pre-defined dwell time which is proportional to the intensity of the 'color' at that location. In this fashion an input pattern is reproduced on the polymer film. Fig. 5(*a*) shows the input image used to reproduce a two-color version of the logo of the Lawrence Berkeley National Laboratory (LBNL). It is composed of a roof pattern in one color (red) and a window/tower pattern in a second color (blue). The red pattern was written into the PMMA layer by selectively damaging the C═O group at 288.4 eV. The blue pattern was written into the PAN layer by selectively damaging the C≡N functional group at 286.8 eV. These patterns were written in the PMMA/PAN bilayer and in the microtomed PECA film. Exposures were 100 ms pixel^{-1} at 288.4 eV with a measured incident flux (I_o) of 2.0 MHz and 200 ms pixel^{-1} at 286.8 eV with $I_o = 2.25$ MHz (note the detector efficiency is ∼30% at these energies, and thus the actual incident photon flux is about three times larger). Under these conditions the estimated dose per pixel at 288.4 eV is 58×10^6 Gy into the PMMA layer and 14×10^6 Gy into the PAN layer, while the estimated dose per pixel at 286.8 eV is 7×10^6 Gy into the PMMA layer and 172×10^6 Gy into the PAN layer. Similar doses would be given to the respective ester and nitrile functional groups of PECA. As shown in Figs. 5(*b*) and 5(*c*), the input patterns were transferred in a chemically selective manner into the PMMA/PAN bilayer film, but not into the PECA film. In the latter case the initial absorption by the C═O groups generates electrons, ions and radicals which transfer the damage to the C≡N groups at the same (x,y) position, and *vice versa*. For PECA, the final generated composite image is a uniform purple color rather than the cleanly color-separated images for the PMMA/PAN bilayer film (Figs. 5*b* and 5*c*).

Several other patterns were further selectively patterned on the PMMA/PAN bilayer as shown in Figs. 5(*d*) and 5(*e*). These patterns are more complicated in that a gray scale within each color is generated by varying the dwell time for each pixel between 0 and 500 ms for PMMA and between 0 and 1000 ms for PAN with ∼1 MHz incident flux to achieve a color gradient of the patterning. High gradient, good chemical contrast and precise overlay of the two separate images were created in the bilayer system. Currently the observed line widths are about 200 nm, even though the STXM beam spot is 45 nm in diameter at the focal spot (Kilcoyne *et al.*, 2003). The increased line width is not due to spatial jitter of the X-ray beam since the position of the beam relative to the sample is controlled interferometrically and is stable to better than 10 nm (Kilcoyne *et al.*, 2003). The possible factors that lead to the broadening of the line width are explored in the following section.

4. Discussion

4.1. What causes the spread of damage beyond the size of the X-ray beam?

Radiation damage to polymers and other materials initiated by soft X-rays is a complicated process with many contributing factors. The initial absorption of a soft X-ray photon excites a core electron at a specific atom in the sample to form a very short-lived (few fs) neutral high-energy excited state. The core hole rapidly relaxes by the Auger process to create a high-energy electron (∼250 eV kinetic energy) and a singly or doubly ionized valence excited state (in principle the core hole can also decay by X-ray fluorescence, but that has negligible probability in the soft X-ray regime). The electronic disturbance in the valence ionized state extends over many bonds,

and has a high probability of breaking one or more bonds to form energetic and very reactive radical/ion fragments. In addition, the Auger electron has a range of ~1 nm and suffers inelastic collisions which ionize other nearby sites. In the picosecond time frame the initially absorbed energy has broken a number of bonds within a few nm of the absorption site, and released a number of energetic electrons and radicals or ions which are capable of further propagating the damage. Although the electrons are damaging, their range is limited to at most a few tens of nanometers owing to their strong interactions in condensed media. It is probably energetic radicals or (less likely) ions that are responsible for the longer-range effects since they are much more damaging and there is the possibility of chain processes. Reaction of these radicals and ions with nearby molecules can create new radicals/ions thereby setting up a chain process which may transfer the damage to regions far (~100 nm) from the initial absorption site. This process can be viewed as radical- or ion-initiated chain depolymerization or fragmentation. If so, it should be susceptible to containment by use of radical scavengers or inhibitors of radical chain reactions. We are presently exploring methods to reduce the line width by addition of radical scavengers (inhibitors) and the use of indirect methods such as chemical amplification.

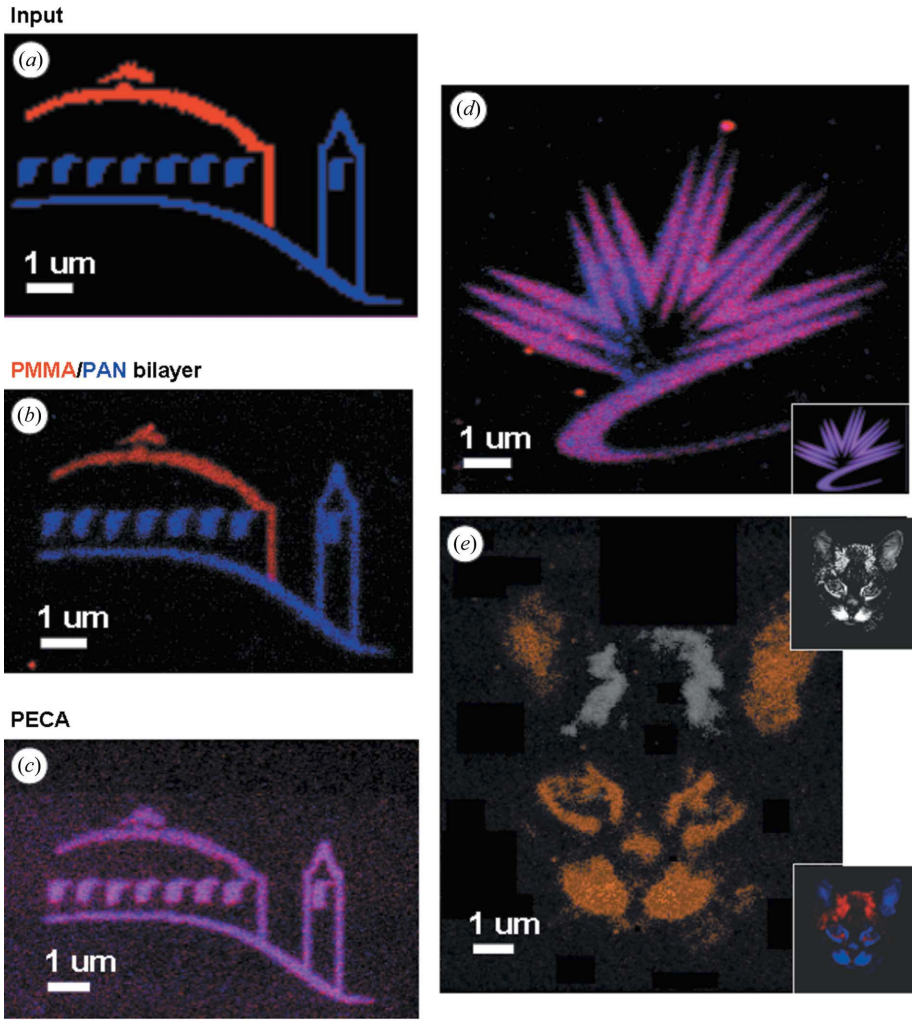

Figure 5
Demonstration of chemically selective patterning for PMMA/PAN bilayer and PECA. (*a*) LBNL logo input file, with the roof in red (PMMA) and the window/tower in blue (PAN). The lower images are color-coded composites derived from STXM images recorded at 286.8 eV (PAN damage, indicated in blue) and 288.4 eV (PMMA damage, indicated in red) of regions of (*b*) the PAN/PMMA bilayer and (*c*) PECA, into which the patterns indicated in (*a*) were written. Gradient patterns selectively generated in the PMMA/PAN bilayer system. (*d*) Logo for the Canadian Light Source (CLS). (*e*) 'Smokie' the cat (photograph courtesy of S. G. Urquhart). A different scheme to colorize the damage was used in this case. The input to make each image is shown as an inset.

Another factor that might contribute is localized heating and associated thermal damage. We have compared widths of the damage line written with the sample under vacuum, where there is very limited thermal dissipation at the sample, with that of lines written using the same dose but with the sample in helium, which provides good thermal dissipation at the sample. The results (Fig. 6) indicate that the line width in a vacuum is the same as that in helium within the measurement uncertainties. This indicates experimentally that the localized heating is low and the thermal damage is negligible. In addition, the temperature rise associated with localized heating was estimated using equation (4) which is an approach developed to describe local heating in TEM in terms of a steady-state model (Egerton *et al.*, 2004),

$$\begin{aligned}\text{Heat} &= \text{Heat}_{\text{conduction}} + \text{Heat}_{\text{radiation}} \\ &= \frac{4\pi\kappa l(T - T_0)}{0.58 + 2\ln(2R_0/d)} + \pi\left(d^2/2\right)\varepsilon\sigma\left(T^4 - T_0^4\right), \quad (4)\end{aligned}$$

where T and T_0 are the temperatures of the local spot and surroundings under steady state, respectively, κ is the thermal conductivity of the polymer, l is the sample thickness, d is the diameter of the assumed circular X-ray spot, R_0 is the distance for thermal conduction, ϵ is the radiation emissivity of the polymer, and σ is the Stefan–Boltzmann constant for radiation. Samples in a TEM are in a high or ultrahigh vacuum, so there is only conduction through the solid to dissipate thermal energy. In contrast, the sample in STXM is normally immersed in a one-third atmosphere of helium, and thus heat dissipation occurs through both the solid and the gas. Thus applying the TEM model for estimating the local heating in STXM will overestimate the possible temperature rise. An estimation of the local temperature rise was made for PMMA under typical conditions used for STXM patterning and assuming 80% of the energy deposited by photoabsorption turns into thermal

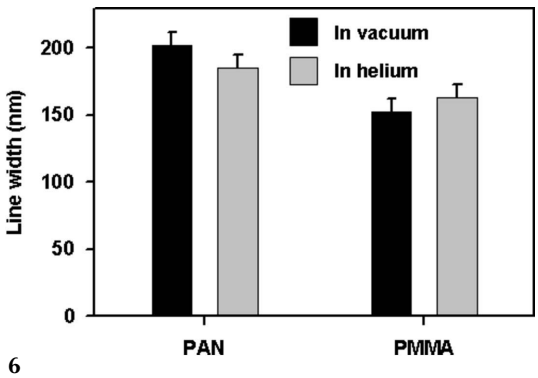

Figure 6
Effect of environment (vacuum *versus* one-third atmosphere of helium) on the line width with adjusted same dose for vacuum and helium for both PMMA and PAN.

energy. The calculation shows that the thermal radiation factor is a few orders of magnitude smaller than thermal conduction and that the temperature rise is only $\sim 5 \times 10^{-4}$ K. Thus the local heating in STXM is much smaller than that in TEM, for which the computed temperature rise under normal imaging conditions is a few degrees Kelvin (Egerton *et al.*, 2004).

4.2. What is the role of the interface in preventing spread of damage between the layers?

While the capability to selectively pattern into PMMA/PAN bilayers has been demonstrated repeatedly, it is puzzling why this works. As Fig. 7 indicates, the range of 'damage transport' resulting in line broadening in the copolymer systems exceeds the thickness of the combined bilayer system. The bonds are not highly aligned (there is no NEXAFS polarization dependence) and thus there is no reason to expect the primary products of the X-ray absorption (photoelectrons, radicals and ions from the first bond-breaking event) to be preferentially directed in the plane of the layer. Even if that was the case, the secondary scattering and chemical reaction events would rapidly erase any initial directional preference. Thus the electrons and radicals/ions should leave the site of the X-ray absorption, which is at the carbon atom of the C═O or C≡N group, with roughly an isotropic angular distribution. Given that expectation, why doesn't the damage generated in one layer spread to the adjacent layer?

The high degree of photon energy selectivity in the PMMA/PAN bilayer, where the X-rays pass through both materials simultaneously, indicates that, even though the thickness of each film (20–40 nm) is much smaller than the range of radical migration in these materials (100–200 nm), the interface between the two layers forms an effective barrier to damage migration, isolating the damage within the separate films. Transmission electron microscopy was used to exclude the possibility of a physical gap between the layers of a bilayer film by viewing the cross section of the bilayer interface. The two layers were in intimate contact (<1 nm). More plausible is the possibility that reactive migrating species are physically trapped in the potential energy well present at the interface between two incompatible polymers. Finally, it may be possible that small amounts of impurities including low-

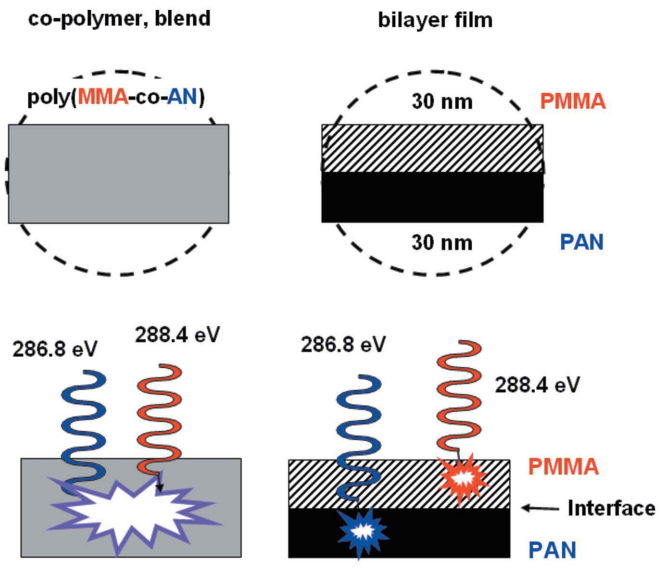

Figure 7
Diagram emphasizing the critical role of the interface in achieving chemically selective patterning by minimizing radical migration between layers.

molecular-weight oligomers were extruded from either or both layers during the spin-coating and drying/annealing process, and were chemically trapping migrating reactive species. Note that there is no spectroscopic evidence for the latter situation: discontinuous impurities at anything more than 2–3 nm thickness would be detected in the images. A continuous layer could be a little thicker (perhaps up to 5–6 nm), but ultimately would show up as a change in the C 1*s* spectra. If interface chemistry is involved, spatial separation alone may not be sufficient for chemically selective damage and patterning on the same region of the bilayer sample. Further analysis of the interface regarding the morphology and composition is needed to understand the role of the interface in quenching the damage spread. This will also help design more advanced systems for chemically selective patterning or lithography.

Although further work is needed to improve spatial resolution and chemical contrast, already this level of chemically selective patterning with STXM allows systematic exploration of potential advantages over other forms of lithography, and provides a platform to explore possible applications. The added value of this technique is chemical selectivity through the use of tuned monochromated synchrotron X-rays. Obvious disadvantages include limited access to focused synchrotron light, expense, and limited spatial resolution. With appropriately prepared layered samples, this technique will allow selective modification of a specific component in a multi-polymer layered system or other multi-component systems. Attributes of possible interest for exploitation include: chemical selectivity, high gradient and contrast patterning, and direct writing of submicrometer patterns on polymer photoresists *etc.* While the ease of tuning, high brightness and highly monochromatic character of the STXM is well suited for method development and demonstrations, practical implementation of this chemically specific lithography will most

likely be carried out using laser plasma or X-ray laser sources which are tuned to the chemically specific energies, combined with full-field X-ray exposure systems, through a suitable mask. A concerted effort is currently under way to develop practical laser-based full-field soft X-ray microscope systems (http://euverc.colostate.edu; http://www.jmar.com), which could be suitable systems in which to implement practical applications of the phenomena we have demonstrated.

Further work to develop multilayer systems, in particular a trilayer system which will allow 'full color' reproduction at the submicrometer scale, is now under investigation. This requires finding a third polymer which has strong absorption at an energy different from the characteristic absorption lines of the PAN and PMMA components, and limited absorption at the PAN and PMMA characteristic energies. In addition, a method of fabricating the trilayer so that each layer is thin and uniform, with minimal mixing of the layers, must be developed. Currently a variety of possible combinations of polymers, solvents and sequence for spin-coating are being explored. Furthermore, an exposure optimization program has been developed which can predict the conditions (photon energies, layer thicknesses, ordering and exposure times) which provide best contrast in any given multilayer system, given knowledge of the absorption spectrum and the critical dose.

In order to improve the spatial resolution of the patterning, it is necessary to understand the origin of the damage spreading, which we currently hypothesize as being associated with radical migration. Preliminary experiments have shown that radical quenchers have some line-narrowing effect, but their influence is relatively minor. A possible explanation is that core-excitation-induced radiation damage leads to a fast cascade process and rapid radical/ion migration and associated chemical and physical changes, which cannot be controlled by a low concentration of radical quenchers. Further exploration of this issue is required.

This research was supported by NSERC (Canada), the Canadian Foundation for Innovation, and the Canada Research Chair Program. X-ray microscopy was carried out at the Advanced Light Source (supported by DoE under contract DE-AC03-76SF00098). We thank David Kilcoyne for expert maintenance of STXM532, Marcia West for superb ultramicrotomy, and Daniel Hernandez-Cruz for assistance with operating the STXM.

References

Ade, H. (1998). *Experimental Methods in the Physical Sciences*, Vol. 32, pp. 225–262. New York: Academic Press.

Ade, H. & Urquhart, S. G. (2002). *Chemical Applications of Synchrotron Radiation*, pp. 1091–1153. River Edge, NJ: World Scientific.

Bauer, E. (2001). *J. Electron Spectrosc. Relat. Phenom.* **114–116**, 975–987.

Beetz, T. & Jacobsen, C. (2003). *J. Synchrotron Rad.* **10**, 280–283.

Cadet, J., Douki, T., Gasparutto, D. & Ravanat, J. L. (2005). *Rad. Phys. Chem.* **72**, 293–299.

Cazaux, J. (1997). *J. Microsc.* **188**, 106–124.

Cerrina, F. (2000). *J. Phys. D*, **33**, R103–R116.

Cherezov, V., Riedl, K. M. & Caffrey, M. (2002). *J. Synchrotron Rad.* **9**, 333–341.

Coffey, T., Urquhart, S. G. & Ade, H. (2002). *J. Electron Spectrosc.* **122**, 65–78.

Egerton, R. F., Li, P. & Malac, M. (2004). *Micron*, **35**, 399–409.

Ekpenyong, K. I. & Okonkwo, R. O. (1983). *J. Chem. Educ.* **60**, 429–430.

Guo, L. J. (2004). *J. Phys. D*, **37**, R123–R141.

Henke, B. L., Gullikson, E. M. & Davis, J. C. (1993). *Atom. Data Nucl. Data Tables*, **54**, 181–342.

Hitchcock, A. P., Morin, C., Heng, Y. M., Cornelius, R. M. & Brash, J. L. (2002). *J. Biomater. Sci. Polym. Ed.* **13**, 919–938.

Jacobsen, C., Wirick, S., Flynn, G. & Zimba, C. (2000). *J. Microsc.* **197**, 173–184.

Joers, J. M., Fong, P. M. & Gore, J. C. (2006). *Phys. Med. Biol.* **51**, N23–N30.

Kilcoyne, A. L. D., Tyliszczak, T., Steele, W. F., Fakra, S., Hitchcock, P., Franck, K., Anderson, E., Harteneck, B., Rightor, E. G., Mitchell, G. E., Hitchcock, A. P., Yang, L., Warwick, T. & Ade, H. (2003). *J. Synchrotron Rad.* **10**, 125–136.

Koprinarov, I. N., Hitchcock, A. P., Li, W. H., Heng, Y. M. & Stöver, H. D. H. (2001). *Macromolecules*, **34**, 4424–4429.

Melngailis, J., Mondelli, A. A., Berry III, I. L. & Mohondro, R. (1998). *J. Vac. Sci. Technol. B*, **16**, 927–957.

Morin, C., Hitchcock, A. P., Cornelius, R. M., Brash, J. L., Urquhart, S. G., Scholl, A. & Doran, A. (2004). *J. Electron Spectrosc.* **137–140**, 785–794.

Osetsky, Y. N. & Bacon, D. J. (2003). *Nucl. Instrum. Methods Phys. Res. B*, **202**, 31–43.

Pease, R. L. (2003). *IEEE Trans. Nucl. Sci.* **50**, 539–551.

Rightor, E. G., Hitchcock, A. P., Ade, H., Leapman, R. D., Urquhart, S. G., Smith, A. P., Mitchell, G., Fischer, D., Shin, H. J. & Warwick, T. (1997). *J. Phys. Chem. B*, **101**, 1950–1961.

Sagstuen, E., Sanderud, A. & Hole, E. O. (2004). *Rad. Res.* **162**, 112–119.

Sanche, L. (2002). *Mass Spectrom. Rev.* **21**, 349–369.

Stöhr, J. (1992). *NEXAFS Spectroscopy*, *Springer Tracts in Surface Science 25*, p. 245. Berlin: Springer.

Stulen, R. H. & Sweeney, D. W. (1999). *IEEE J. Quant. Electron.* **35**, 694–699.

Trachenko, K. (2004). *J. Phys. Condens. Matter*, **16**, R1491–R1515.

Tseng, A. A., Chen, K., Chen, C. D. & Ma, K. J. (2003). *IEEE Trans. Electron. Pack. Manuf.* **26**, 141–149.

Tseng, A. A., Notargiacomo, A. & Chen, T. P. (2005). *J. Vac. Sci. Technol. B*, **23**, 877–894.

Wang, J., Morin, C., Li, L., Hitchcock, A. P., Scholl, A. & Doran, A. (2007). *J. Electron. Spectrosc. Relat. Phenom.* Submitted.

Warwick, T., Ade, H., Kilcoyne, A. L. D., Kritscher, M., Tylisczcak, T., Fakra, S., Hitchcock, A. P., Hitchcock, P. & Padmore, H. A. (2002). *J. Synchrotron Rad.* **9**, 254–257.

Weik, M., Ravelli, R. G. B., Kryger, G., McSweeney, S., Raves, M. L., Harel, M., Gros, P., Silmani, I., Kroon, J. & Sussman, J. L. (2000). *Proc. Natl. Acad. Sci.* **97**, 623–628.

Zhang, X., Jacobsen, C., Lindaas, S. & Williams, S. (1995). *J. Vac. Sci. Technol. B*, **13**, 1477–1483.